# High-Fidelity Aerodynamic Shape Optimization of a Lifting-Fuselage Concept for Regional Aircraft

Thomas A. Reist* and David W. Zingg†

*Institute for Aerospace Studies, University of Toronto*

*4925 Dufferin St., Toronto, Ontario, M3H 5T6, Canada*

**High-fidelity aerodynamic shape optimization based on the Reynolds-averaged Navier-Stokes equations is used to optimize the aerodynamic performance of a conventional tube-and-wing design, a hybrid wing-body (HWB), and a novel lifting-fuselage concept for regional-class aircraft. Trim-constrained drag minimization is performed on an HWB design, with an optimized conventional design serving as a performance reference. The optimized regional-class HWB yields no drag savings when compared to the conventional reference aircraft. Starting from the optimized HWB, an exploratory optimization with significant geometric freedom is then performed, resulting in a novel shape with a slender lifting fuselage and distinct wings. Based on this exploratory result, a new regional-class lifting-fuselage configuration is designed and optimized. With a span constrained by code 'C' gate limits and having the same wing-only span as the conventional reference aircraft, this new design produces up to 10% lower drag than the reference aircraft. The effect of structural weight uncertainties, cruise altitude, and stability requirements are also examined.**

## Nomenclature

| | |
|---|---|
| CTW | Conventional tube-and-wing |
| HWB | Hybrid wing-body |
| LFC | Lifting-fuselage configuration |
| $x$, $y$, $z$ | Streamwise, spanwise and vertical coordinates |

*Ph.D. Candidate, AIAA Student member, tom.reist@utoronto.ca

†Professor and Director, J. Armand Bombardier Foundation Chair in Aerospace Flight, Associate Fellow AIAA, dwz@oddjob.utias.utoronto.ca

| | |
|---|---|
| $c$ | Local chord length |
| MAC | Mean aerodynamic chord |
| $b$ | Total aircraft span |
| $S$ | Reference planform area |
| $t/c$ | Section thickness normalized with local chord length |
| $q_\infty$ | Freestream dynamic pressure |
| $C_p$ | Coefficient of pressure |
| $L$, $D$, $M$ | Total lift, drag, and pitching moment of the aircraft |
| $C_L$, $C_D$, $C_M$ | Total lift, drag, and pitching moment coefficients of the aircraft |
| $C_{D_p}$, $C_{D_f}$ | Coefficients of pressure and friction drag |
| $L/D$ | Lift-to-drag ratio |
| $K_n$ | Static margin, $-\partial C_M/\partial C_L$ |
| $W$ | Aircraft weight |
| MTOW | Maximum take-off weight |
| OEW | Operating empty weight |
| CG | Center of gravity |
| $\Delta x_{\text{CG}}$ | Streamwise movement of the center of gravity |
| $N$ | Number of CFD grid nodes |

# I. Introduction

Although there have been great advances in transport aircraft efficiency since the introduction of the de Havilland Comet in 1952, the conventional tube-and-wing (CTW) configuration remains to this day. Performance improvements have come from modifications to aerodynamic design, such as the use of winglets and supercritical airfoils, as well as high performance materials and increasingly fuel efficient engines. However a step change in fuel efficiency may be possible through novel configurations. One such configuration that has received much attention in recent years is the blended, or hybrid, wing-body (HWB). This design combines the aircraft fuselage and wings into one tightly integrated airframe with improved aerodynamic, structural, propulsive, and acoustic efficiency.

The HWB has the potential to be more aerodynamically efficient than conventional configurations, largely due to the increased span allowed for by the broad payload-carrying center-body.[1] The overall shape of the HWB is also cleaner than a conventional design, leading to reduced interference drag. Structurally, the aerodynamic lifting loads are more closely aligned with the weight of the aircraft due to the lifting fuselage,

leading to reduced bending loads in the main wing structure and therefore potentially lower structural wing weight and increased span.[1] The use of a well integrated propulsion system, such as boundary-layer-ingestion or distributed propulsion, can lead to propulsive efficiencies. A well integrated propulsion system on the top of the aircraft can also provide significant noise reductions due to the acoustic shielding provided by the aerodynamic surfaces.[2] The highly integrated nature of the design allows for efficiency improvements; however this also increases the design challenges stemming from such a tightly coupled configuration.

One of the main structural challenges associated with the HWB is the lack of the efficient cylindrical pressure vessel present in conventional designs. Much work has been dedicated to the design of efficient structural concepts and composites tailored for handling these pressure loads.[3–5] Due to its tailless nature, stability and control can be challenging with this design. Work has been done on addressing some of these issues.[6,7] With such a radically different design, certification and customer acceptance must also be addressed. Finally, perhaps the biggest obstacle to the development of the HWB is the financial risk associated with pursuing such a novel design. However, with increasing concern about aviation's environmental impact, the potential benefits of this unconventional design may justify its development.

Several large projects around the world have focused on the development of the HWB design. In the United States, Boeing and NASA have been involved in the identification and development of enabling technologies required for the HWB design,[1,3,4,6,8,9] with contributions leading to the X-48 flight demonstrators. An HWB design focused on noise reduction has been developed as part of Cambridge and MIT's 'Silent' Aircraft Initiative.[2,10] In Europe, two of the main projects relating to HWB design are the Multidisciplinary Optimization of an HWB (MOB)[11] and the Very Efficient Large Aircraft (VELA)[12] projects.

Aerodynamic shape optimization has been applied to the HWB design at a variety of fidelity levels. Peigin and Epstein[13] used a Navier-Stokes solver and genetic optimizer for the optimization of the MOB configuration for multiple operating points with airfoil, dihedral and twist design variables. Qin et al.[14] performed spanload optimization through twist modification as well as 3D surface optimization using both Euler and Navier-Stokes solvers. Both airfoil and sweep optimization were performed by Le Moigne and Qin[15] using a discrete adjoint method with an Euler solver. They demonstrated that the imposition of pitching moment constraints has a large impact on the optimal shape, yet only a small performance penalty must be paid. The performance improvements obtained using Euler-based optimization are also realized when evaluated with a Reynolds-averaged Navier-Stokes (RANS) solver. The challenge of considering stability and control of flying-wings during aerodynamic shape optimization has been addressed by Mader and Martins[16] through the application of a time-spectral method for optimizing in the presence of static and dynamic stability constraints. A small HWB was optimized by Kuntawala et al.[17] using a large number of geometric design variables for full 3D surface optimization. More recently, Lyu and Martins optimized an 800 passenger

HWB using both the Euler[18] and RANS[19] equations subject to trim, static-stability, and root bending-moment constraints. Previous work by the present authors includes single and multipoint optimization of a regional-class HWB using both the Euler and RANS equations.[20] The impact of trim and stability constraints on the optimal HWB design at both on- and off-design conditions was examined. It was demonstrated that, for cruise, these constraints lead to a small performance penalty at on-design conditions through tailoring of the aerodynamic shape and aircraft weight distribution, while performance degrades significantly at off-design conditions. It was also shown, as with the work of Osusky and Zingg,[21] the necessity of using the RANS equations for aerodynamic design in order to not only capture the viscous components of drag, but also to properly determine and control the local flow behaviour.

Historically, the focus of HWB design investigations has been on large capacity aircraft in the 400-1000 passenger range. The HWB's intrinsic design features lend themselves well to large aircraft. While the HWB's suitability for smaller aircraft is often dismissed, little public work has been done to establish this. Nickol examined a series of HWB aircraft ranging from 98-400 passengers.[8] The fuel burn benefit was most significant for the larger aircraft, with the 98 passenger aircraft burning more fuel than a comparable tube-and-wing aircraft. However, the fuel burn disadvantage of the small HWB was highly sensitive to drag. Thus, if a suitable drag reduction can be achieved through aerodynamic shape optimization, perhaps resulting in a shape significantly different than that assumed by Nickol, the HWB could potentially be more fuel efficient than the tube-and-wing aircraft for a variety of aircraft classes. While high-fidelity aerodynamic shape optimization has been applied extensively to large HWBs as shown above, its use in the design of smaller aircraft has received less attention. The objectives of this paper are to use high-fidelity aerodynamic shape optimization to evaluate the optimal aerodynamic performance of HWB aircraft relative to equivalently optimized conventional tube-and-wing designs for regional-class aircraft, and to explore alternatives to the HWB configuration which may yield improved efficiency for this class of aircraft.

This paper is structured as follows. Section II presents the design problem that is to be investigated, including class and mission specification. Baseline designs are created and sized using a low-fidelity tool. Section III describes the aerodynamic shape optimization setup and the optimization results for the baseline designs. Section IV presents the results of an exploratory aerodynamic shape optimization with increased geometric freedom, and the design of a new lifting-fuselage configuration (LFC) that is more efficient than the baseline. Section V presents structural weight sensitivity studies as well as examines the impact of cruise altitude on performance and the impact of longitudinal static stability requirements.

## II. Design Problem

Both CTW and HWB configurations are considered in this work, where the CTW design serves as a performance reference for the HWB designs. A regional-class aircraft is considered, with a single-class capacity of 100 passengers and a maximum range capability of 3,000 nmi plus reserves. This is similar to the design mission of the Embraer E190. The nominal mission, at which the aircraft will be optimized, is a single-stage 500 nmi mission with full passenger payload at 36,000 ft and Mach 0.78.

Both the CTW and HWB baseline designs are developed using a low-fidelity tool that incorporates aerodynamic and weight-and-balance analyses using the methods of Torenbeek,[22] Kroo,[23] and Raymer.[24] No optimization is performed with this tool, but rather, for a specified design layout and mission profile, the tool provides weight and center of gravity (CG) information for use in the high-fidelity optimization. For the HWB designs, the weight of the center-body structure is obtained using the method of Bradley.[25] The methods used to obtain the remaining structure, systems, fuel, and operational item weights for the HWB are the same as those used for the CTW aircraft. The same low-fidelity aerodynamic models are used for both aircraft, with the HWB being treated as a wing. This weight estimation methodology has been evaluated for a series of CTW designs against publicly available data, and for HWB aircraft against the results of Nickol.[8] Details of each design are presented below, with all estimates based on technology levels similar to those of the E190, upon which the reference aircraft is based. The methods used to choose the mission profiles and to develop the baseline designs are very low-fidelity and do not represent full system-optimal design or operation.[a] Instead, they are meant only to serve as a reasonable starting point for the high-fidelity optimization. All performance comparisons will be made based on the high-fidelity optimized designs.

### A. Baseline Conventional Tube-and-Wing Design

The baseline CTW design, referred to as the CTW100, is modeled after the Embraer E190 using publicly available data.[26] Estimates for aircraft weight and performance are obtained via the methods described above. The low-fidelity model of the baseline design is shown in Figure 1 with the corresponding design information given in Table 1. These models assume an engine similar to that used on the E190, the General Electric CF34-10E series.[27] Two engines are used, each with a weight of 3,700 lb, and cruise TSFC of 0.64. This information is used solely for sizing of the initial configurations.

[a] While there is uncertainty in the weight estimates, particularly for the HWBs, it should be noted that the HWB weights relative to the CTW are similar to those of Nickol, i.e. both Nickol's HWBs and those presented here are heavier than their CTW equivalents. A direct comparison is not possible due to Nickol's use of advanced technologies not considered here.

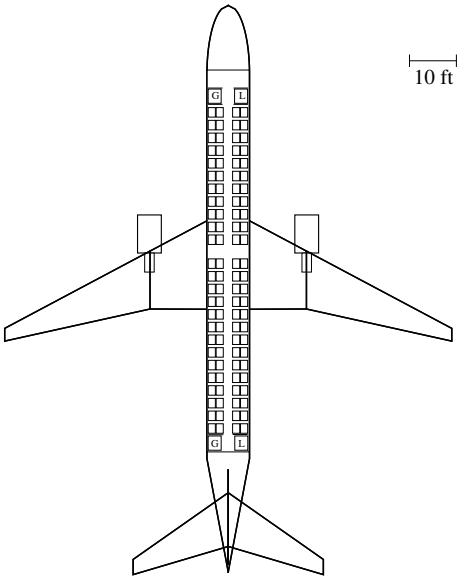


**Figure 1: Baseline CTW100 design.**

**Table 1: Baseline CTW100 design summary.**

| | | |
|---|---|---|
| **Capacity** | | |
| Passengers + crew | 100+5 | |
| Max payload | 28,400 | lb |
| Cargo volume | 800 | $ft^3$ |
| **Geometry** | | |
| Reference area | 1,000 | $ft^2$ |
| Total span | 94 | ft |
| Length | 119 | ft |
| MAC | 13.1 | ft |
| Aspect ratio | 8.8 | |
| **Weight** | | |
| MTOW | 105,800 | lb |
| OEW | 59,200 | lb |
| Wing load at MTOW | 106 | $lb/ft^2$ |
| **Nominal mission cruise** | | |
| Range | 500 | nmi |
| Altitude | 36,000 | ft |
| Mach number | 0.78 | |
| Reynolds number | 23 | $\times 10^6$ |
| Weight* | 91,500 | lb |
| $C_L$* | 0.45 | |
| CG location* | 55 | ft |

* At start of cruise

## B. Baseline Hybrid Wing-Body Design

The baseline HWB design, referred to as the HWB100, resembles a 'classic' HWB shape, i.e. similar to a scaled-down version of Liebeck's[1] designs and those used by Nickol.[8] The span is chosen to be 118 ft to comply with ICAO code 'C' gate requirements. The assumption is made that the HWB designs will require some form of lateral stabilizer. It is assumed that two vertical stabilizers, or fins, outboard of the engines will be used so as to provide noise shielding, as shown in Figure 2. These stabilizers are sized such that they have sufficient area to counteract a one-engine-inoperative yawing moment, given the same fin lift coefficient as the baseline conventional aircraft. The interior cabin height is 78 inches, the same as that of the CTW. The same engines are used for the HWB as for the CTW, where simple pylon mounting is assumed such that the HWB receives no credit for advanced engine installation, such as boundary layer ingestion. A summary of the design is given in Table 2.

Full 3D surface models of the baseline designs are created using the geometry toolbox developed by Gagnon and Zingg[28] and are shown in Figure 3. The baseline CTW wing is untwisted and uses the SC(2)-0012 section at the root and SC(2)-0010 at the tip. The baseline HWB body uses SC(2)-0014 sections, with SC(2)-0012 and SC(2)-0010 sections at the wing root and tip, respectively. Since the initial center-body airfoils are not designed specifically for HWB use, in order to maintain sufficient thickness up to 70% chord to house the cabin, a 14% thick section is used on the center-body. This is an inefficient packing of the cabin

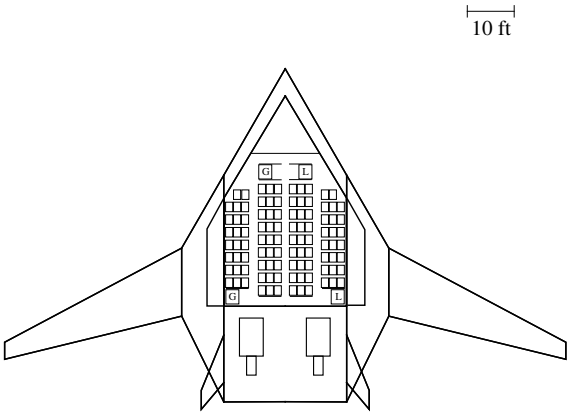


**Figure 2: Baseline HWB100 design.**

**Table 2: Baseline HWB100 design summary.**

| | | |
|---|---|---|
| **Capacity** | | |
| Passengers + crew | 100+5 | |
| Max payload | 28,400 | lb |
| Cargo volume | 800 | $ft^3$ |
| **Geometry** | | |
| Reference area | 2,734 | $ft^2$ |
| Total span | 118 | ft |
| Length | 70 | ft |
| MAC | 42.4 | ft |
| Aspect ratio | 5.1 | |
| **Weight** | | |
| MTOW | 117,700 | lb |
| OEW | 70,200 | lb |
| Wing load at MTOW | 43.1 | $lb/ft^2$ |
| **Nominal mission cruise** | | |
| Range | 500 | nmi |
| Altitude | 36,000 | ft |
| Mach number | 0.78 | |
| Reynolds number | 76 | $\times 10^6$ |
| Weight* | 103,200 | lb |
| $C_L$* | 0.19 | |
| CG location* | 41 | ft |

* At start of cruise

within this section, so the optimizer will be used to design a more appropriate section that has a smaller maximum thickness-to-chord ratio, which is maintained over a larger fraction of the chord. The initial section does not affect the converged result, as the optimizer has a large amount of geometric freedom; the optimal section shape is largely driven by the cabin shape constraint, as will be discussed in Section B. These high-fidelity models do not include any vertical stabilizers in order to simplify grid generation, and because their size and shape are determined by flight conditions that are not considered in the optimization. However, the effect of the vertical stabilizers, including weight and drag, is included in the low-fidelity sizing, and their profile drag contribution is accounted for by performing RANS flow analyses on the vertical stabilizers in isolation and adding this contribution to the drag of the optimized designs. The interference drag of the vertical stabilizers and fuselage/center-body is not accounted for as there is large uncertainty in the vertical fin sizing process since it only accounts for a one-engine-inoperative condition, and it is thus assumed that the interference drag would be within the uncertainty of the profile drag. Unless stated otherwise, all results presented in this paper include the effect of the vertical stabilizers.

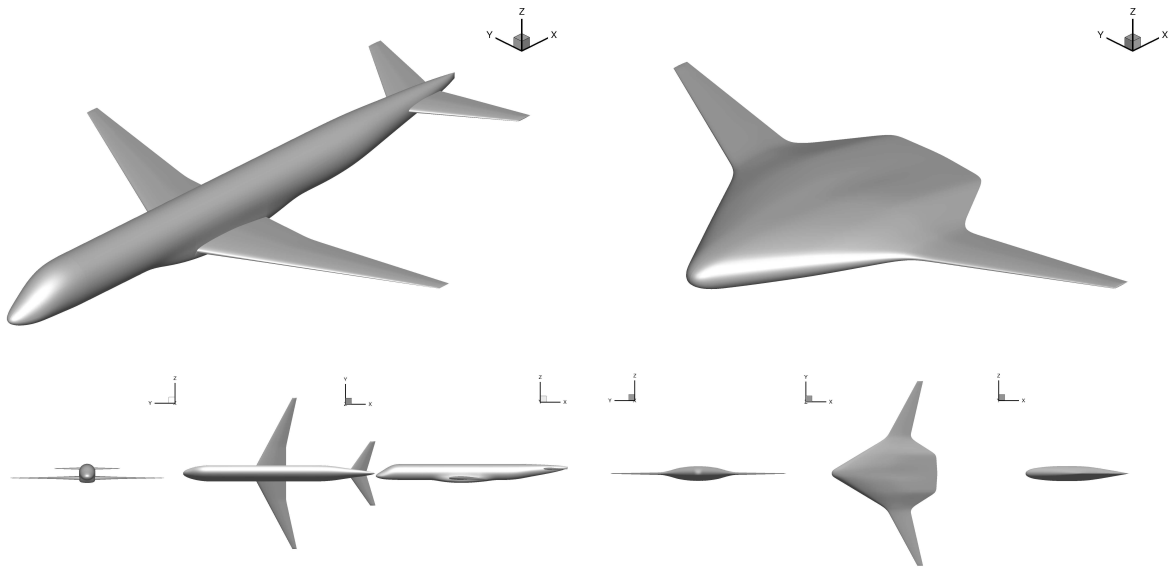

(a) Baseline CTW100 (b) Baseline HWB100

**Figure 3: Full 3D models of the CTW and HWB baseline designs.**

# III. Aerodynamic Shape Optimization

## A. Aerodynamic Shape Optimization Framework

The aerodynamic shape optimization (ASO) algorithm used comprises three main components: 1) a multi-block Newton-Krylov-Schur solver for the Euler[29] and RANS equations with the one-equation Spalart-Allmaras turbulence model,[30] 2) a B-spline geometry parameterization which is coupled with an integrated linear elasticity mesh movement strategy,[31] and 3) the gradient-based optimizer SNOPT[32] with gradients calculated using the discrete adjoint method.[31,33]

The flow solver is a parallel implicit solver that uses summation-by-parts operators for spatial discretization and simultaneous approximation terms for the imposition of boundary conditions and block interface conditions. The Krylov subspace method Generalized Minimum Residual (GMRES) is used with approximate Schur preconditioning in an inexact Newton method for the solution of the discrete equations. Details of the flow solver can be found in Hicken and Zingg[29] and Osusky and Zingg.[30] The flow solver has been validated through participation in the 5$^{\text{th}}$ AIAA Drag Prediction Workshop.[34]

At each optimization iteration for which a geometric shape change occurs, the computational grid must be moved to reflect this change. To accomplish this, each block of the computational grid is fitted with a B-spline volume. The design variables for the optimization can be either the B-spline control points on the aerodynamic surface, or the B-spline parameterization can be embedded within a free-form deformation volume that can be controlled through 'axial curves', as described by Gagnon and Zingg.[35] For this work direct control of the B-spline control points is used. As the B-spline control points on the aerodynamic

surface are moved, each B-spline volume block is treated as a linear elastic solid, for which a finite-element solution is obtained to define the new shape of the B-spline volume. The computational grid is then recovered from this new B-spline volume. This method has been found to be very robust for large shape changes while being relatively inexpensive. Details can be found in Hicken and Zingg.[31]

Due to the high cost of evaluating the flow equations, a gradient-based optimizer is used for optimization, as gradient-based optimizers typically require fewer function evaluations than genetic algorithms.[36] The penalty paid is that for multimodal optimization problems only a local optimum may be found. This can be addressed using the gradient-based global optimization techniques proposed by Chernukhin and Zingg.[37] However, such an approach is not used here. The gradients of the objective and constraints are evaluated using the discrete adjoint method. This method is advantageous for problems with many more design variables than constraints, as the cost of the gradient evaluation is nearly independent of the number of design variables. The number of adjoint solutions required is proportional to the number of objectives and constraints which depend on the flow properties. Since this can require significant computational cost for practical problems, an efficient method of solving the linear system of the adjoint problem is required. For this, a modified, flexible version of the Generalized Conjugate Residual with Orthogonalization and Truncation (GCROT) algorithm is used.[38] The gradient-based optimizer SNOPT is used, as it allows for the solution of large-scale constrained problems. Details of the adjoint method and its integration with the flow solver and mesh movement are given by Hicken and Zingg,[31] while the details of SNOPT are described by Gill et al.[32]

The above algorithm has been used extensively for ASO of various problems including the benchmark validation problems of the AIAA Aerodynamic Design Optimization Discussion Group,[39–41] induced drag minimization of non-planar wings,[35,42] optimization of wings in transonic[35,43] and turbulent flows,[33] the design of low-sweep wings,[44] investigation of the multimodality of ASO problems,[37] and the optimization of unconventional[28,45] and HWB[17,20,46] aircraft. This framework has also been extended to aerostructural optimization.[47,48]

### B. Optimization Problem Formulation

Starting from the 3D models shown in Figure 3, high-fidelity aerodynamic shape optimization is performed at conditions that correspond to the start of the cruise segment of the nominal mission. The starting geometries, which have untwisted wings and use symmetric sections, are initially infeasible and have poor performance. The objective of the optimization is to minimize drag subject to lift and pitching moment constraints, in addition to geometric constraints described below. This work investigates aerodynamically optimal configurations that offer minimum drag for this class of aircraft. Naturally, aircraft design is driven

by additional considerations, such as weight, which would also need to be taken into account during design. Since aerodynamic performance is tightly coupled to other disciplines, the optimization problem design variables and constraints are constructed so as to limit geometric changes which have a significant impact on other disciplines, while allowing enough freedom to achieve aerodynamically optimal designs.

The surface CFD grid and the geometry parameterization are shown in Figure 4. The background surface shows the CFD grid, while the foreground surface shows the B-spline control grid, and the locations of the different geometric design variables are indicated. The design variable definition is consistent with that described in Osusky et al.[33] The specific design variables and constraints are summarized in Table 3 and described below. A portion of the HWB body upper surface is transparent to show the cabin shape. The HWB's internal cabin height is 78 inches, to which a 6 inch buffer is added on both the bottom and top of the cabin to provide space for the structure. This combined volume is enclosed by the cabin shape surface shown in Figure 4.

The angle-of-attack is a design variable for both configurations and is limited to $\pm 3^\circ$ due to deck angle requirements. The incidence angle of the CTW wing and tail are free to vary between $\pm 5^\circ$. For the CTW, the wing chord and twist are allowed to vary at the crank and tip, with linear variation between. For the HWB, the chord is variable at the centerline, and the chord and twist are variable at the outboard edge of the cabin, wing root, and tip, with linear variation between. The CTW and HWB have section control at 12 and 18 span-stations respectively, at each of which there are 22 section variables, 11 for each of the lower and upper surfaces. For each pair of lower and upper surface section shape variables there is a corresponding thickness constraint to prevent the thickness decreasing by more than 20% of the initial value. For the CTW, geometric changes to the fuselage caused by changes of the wing/tail root are handled via the method described in Osusky et al.[33] The CTW wing is divided into two segments, one inboard and one outboard of the crank. The HWB consists of three segments, one over the cabin, one transition segment between the edge of the cabin and the wing root, and one for the wing. The span of each of these segments can vary, but the total span remains fixed. The quarter-chord sweep of the CTW wing and the HWB wing is fixed. The sweep of the transition region of the HWB, between the cabin and the wing, is free to vary such that the optimizer can position the wing to minimize trim drag. The volume of both the CTW and HWB wings is constrained such that sufficient volume exists in the wings for up to 30,000 lb of fuel, a conservative estimate based on the low-fidelity sizing results. It is assumed that 80% of the outer mold line volume is usable for fuel tanks. The outer mold line of the HWB is constrained such that it does not violate the specified HWB cabin shape, shown in Figure 4b.

Lift is constrained to be equal to the weight at the start of cruise, and the pitching moment about the center of gravity must be zero. There are a total of 273 effective design variables for the CTW, and 408 for

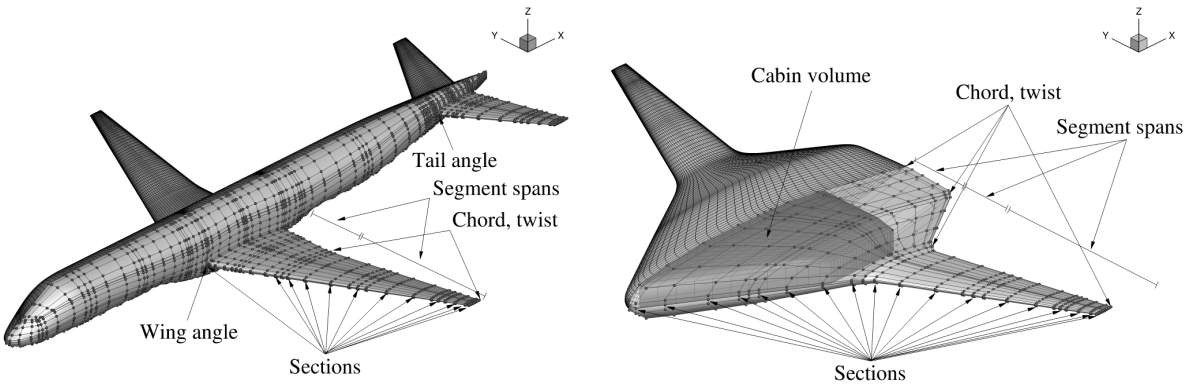


(a) CTW design variables

(b) HWB design variables

**Figure 4: Surface geometries for the CTW and HWB baselines showing both the surface CFD mesh and control mesh along with the types and locations of the geometric design variables. The upper surface of the HWB body is translucent to reveal the polyhedron that encloses the cabin. (Not shown to the same scale.)**

**Table 3: Design variables and constraints. Bounds given as percentages are deviations from the initial values. Numbers in parentheses are the number of each type of variable/constraint.**

| | CTW | | | HWB | | |
|---|---|---|---|---|---|---|
| Variables | $-3° \leq$ | AoA (1) | $\leq +3°$ | $-3° \leq$ | AoA (1) | $\leq +3°$ |
| | $-5° \leq$ | Wing angle (1) | $\leq +5°$ | | | |
| | $-5° \leq$ | Tail angle (1) | $\leq +5°$ | | | |
| | $-75\% \leq$ | Segment span (2) | $\leq +75\%$ | $-75\% \leq$ | Segment span (3) | $\leq +75\%$ |
| | | | | $0° \leq$ | Transition region sweep (1) | $\leq 85°$ |
| | $-50\% \leq$ | Chord (2) | $\leq +50\%$ | $-50\% \leq$ | Chord (4) | $\leq +50\%$ |
| | $-10° \leq$ | Twist (2) | $\leq +10°$ | $-10° \leq$ | Twist (3) | $\leq +10°$ |
| | $-200\% \leq$ | Section shape*(264) | $\leq +200\%$ | $-200\% \leq$ | Section shape*(396) | $\leq +200\%$ |
| | Total effective design variables: 273 | | | Total effective design variables: 408 | | |
| Constraints | $-20\% \leq$ | $t/c$ (132) | $\leq +50\%$ | $-20\% \leq$ | $t/c$ (198) | $\leq +50\%$ |
| | $1.25V_{\text{fuel}} \leq$ | $V_{\text{wing}}$ (1) | | $1.25V_{\text{fuel}} \leq$ | $V_{\text{wing}}$ (1) | |
| | $-0\% \leq$ | Span (1) | $\leq +0\%$ | $-0\% \leq$ | Span (1) | $\leq +0\%$ |
| | $-0\% \leq$ | Sweep (2) | $\leq +0\%$ | $-0\% \leq$ | Sweep (2) | $\leq +0\%$ |
| | | | | | Cabin shape (2050) | |
| | | $L = W$ (1) | | | $L = W$ (1) | |
| | | $C_M = 0$ (1) | | | $C_M = 0$ (1) | |

* The amount by which the control points defining the sections can move normal to the chordline, as a percentage of their initial distance from the chordline.

the HWB. The lift target is not updated during the optimization in response to geometric changes. While changes to weight during the optimization could be captured using the relations used for initial sizing, which are primarily functions of geometry, this is not done due to uncertainties in the accuracy of these equations. These inaccuracies could be exploited by the optimizer to lighten the aircraft in a way which is unrealistic. The aim is to avoid contaminating the high-fidelity optimization with low-fidelity approximations which can be exploited by the optimizer. As a check, after each optimization, new low-fidelity models are built to reflect any geometric changes, and the resulting changes in OEW are typically less than 2%.

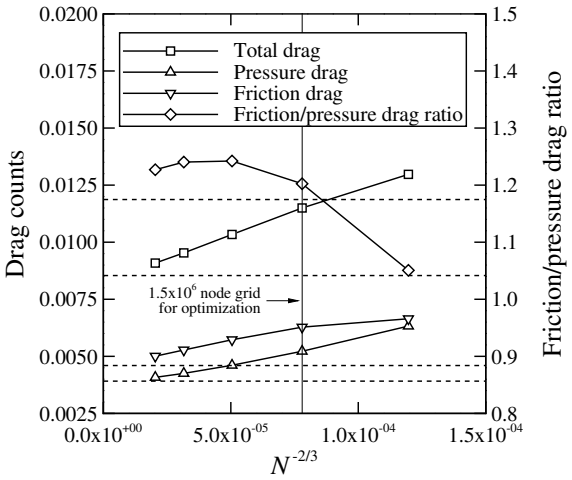


**Figure 5: Grid refinement study on the HWB100-0 design which has been optimized to be shock-free. The dashed horizontal lines indicate the Richardson extrapolated values.**

For RANS-based optimization problems with free wing area it is critical that the ratio of induced and friction drag is predicted accurately such that the optimizer can properly trade friction drag for induced drag by changing the wing area. A grid study is conducted to ensure that the grids used for optimization accurately predict this ratio. First, trim-constrained drag minimization is performed on the HWB100 subject to the problem formulation described above, but with only section and twist variables active, resulting in what will be referred to as the HWB100-0 design. This allows the optimizer to remove shocks, and hence the wave drag contribution to pressure drag. A grid convergence study is then performed on this result, with the grid convergence behavior shown in Figure 5 for grids ranging from 764,000 to $11\times10^6$ nodes. The grid-converged friction/pressure drag ratio, $C_{D_f}/C_{D_p}$, is 1.17, and the $1.5\times10^6$ node grid gives a ratio of 1.20. Thus the $1.5\times10^6$ node grid, indicated in Figure 5, is used for the optimizations. The CTW grid is then created with the same surface resolution; which yields a $6.3\times10^6$ node grid. The local grid node distribution is based on the results of studies examining the effects of local refinement on numerical error. The results of these studies are largely in-line with the guidelines of the AIAA Drag Prediction Workshops.[49] The optimization level grids have off-wall spacings of $y^+ \approx 1.0$, leading and trailing edge spacings of $\approx 0.15\%$ chord, and HWB root and tip spacings of $\approx 0.5\%$ and $\approx 0.02\%$ semi-span, respectively, which are refined for the CTW at the wing-body and tail-body junctions. While these grids are too coarse to provide accurate force and moment estimates, it has been found that they are capable of capturing the dominant flow features and thus properly designing the shape.[37,50]

In order to determine the final force and moment coefficients of the optimized designs, grid convergence studies are performed for each optimized design. For each design a sequence of three grids with 2, 4, and 8 times as many nodes as the optimization grid is created, and Richardson extrapolation is used with an assumed order of accuracy of 2 to determine the grid-converged performance estimates. All results presented

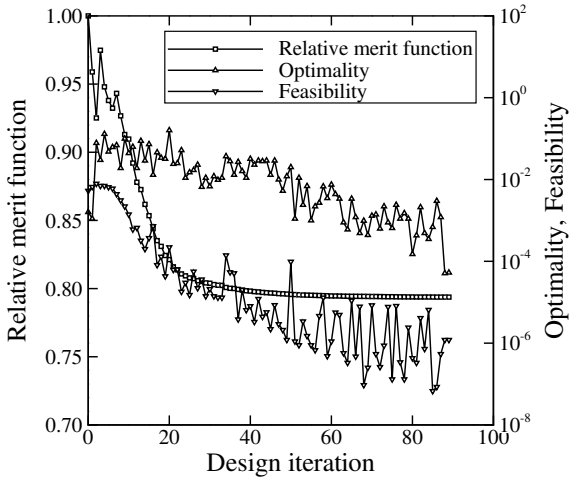


**Figure 6: Optimization convergence history for the HWB100-1 optimization.**

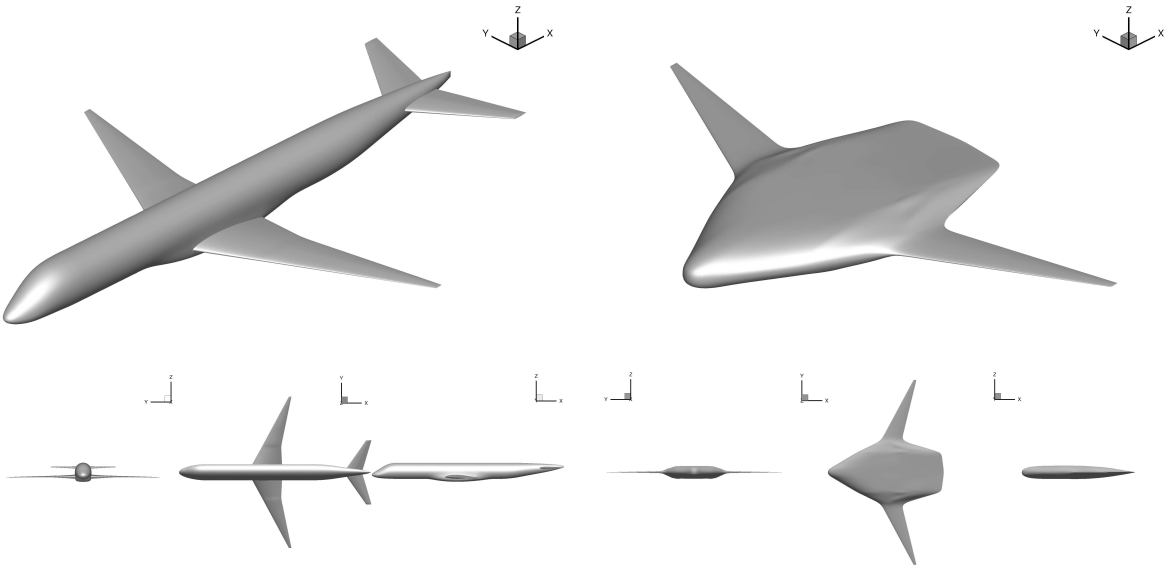

(a) Optimized CTW100-1 (b) Optimized HWB100-1

**Figure 7: Optimized CTW100-1 and HWB100-1 designs.**

in this paper are based on such grid convergence studies.

### C. Optimization Results

Each optimization is run until all constraints are satisfied and there is no longer improvement in the objective function between iterations. The resulting optimized designs for both the CTW and HWB will be indicated by the suffix '-1'. The optimization convergence history for the HWB100-1 optimization is shown in Figure 6. The resulting shapes for both aircraft are shown in Figure 7.

For the CTW100-1 optimization, the optimizer adds washout to reduce induced drag and modifies the

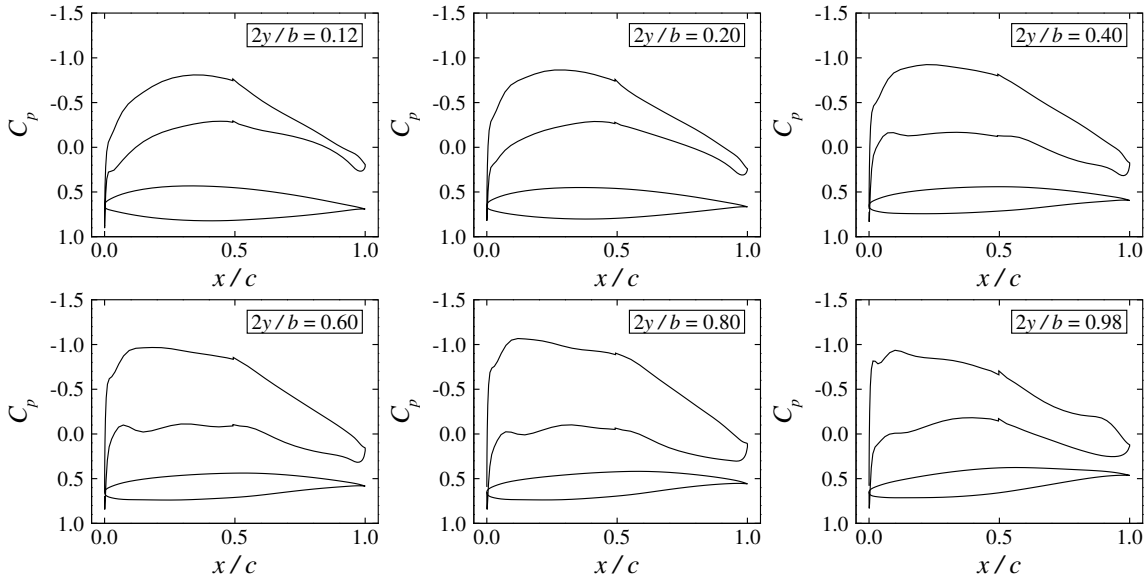


**Figure 8: Pressure distributions at a series of span-stations of the optimized CTW100-1.**

sections to remove any shocks, as evidenced by the pressure distributions in Figure 8.[b] The resulting designs are shock-free and nearly separation-free, where a small recirculation region is present at the trailing edge of the tail-body junction. The wing area is decreased by 6.6%.

For the HWB100-1, the action of the optimizer is to closely wrap the outer mold line of the body around the prescribed cabin shape to minimize wetted area while both increasing the centerline chord on the center-body by almost 10% and reducing the height in order to decrease the maximum thckness to chord ratio to 11%. The HWB100-1 center-body carries 43% of the total lift. Washout is added to the wing, and the sections along the span are shaped to eliminate shocks and remove separation as shown in Figure 9. The pressure profiles also demonstrate the manner in which the optimizer trims the HWB100-1. The center-body sections are fore-loaded such that they carry almost all of their lift ahead of the center of gravity, located at approximately 53% of the centerline chord. Thus no inefficient reflex is required at any position along the span. The optimizer has found the same trim mechanism as described by Sargeant et al.[51] However, the design is longitudinally unstable with a static margin of $-3.8\%$ and would require some form of an active stability system.

### D. Increased Span HWB

The span of the HWB100 design is 118 ft. Due to the span-loading caused by the layout of the passenger compartment, the portion of the span subjected to primarily bending loads, i.e. the 'bending span', decreases relative to the CTW100 configurations. In this paper the bending span will be taken as the span of the

[b]The small pressure discontinuities seen at the mid-chord are due to the presence of a block boundary and the use of simultaneous approximation terms (SATs) for the interface boundary conditions.

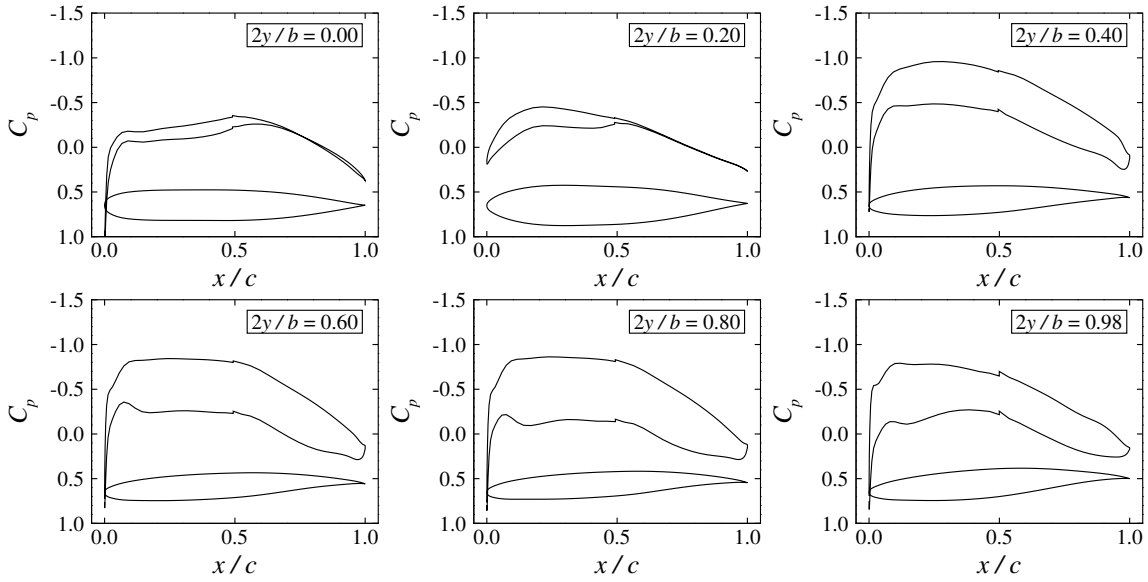


**Figure 9: Pressure distributions at a series of span-stations of the optimized HWB100-1. Station $2y/b = 0.00$ is at the centerline, station $2y/b = 0.20$ is at the outboard edge of the passenger cabin, and the remainder are on the wing.**

wing in isolation and will be used as a low-order surrogate for wing weight. This is conservative with respect to HWB performance since the HWB center-body carries a significant portion of the lift, thus relieving the wing. The CTW100 designs have a bending span of 85 ft, and that of the HWB100 is 76 ft. Thus, a second HWB configuration, referred to as the HWB100D[c], is created with a 130 ft span, such that it has a bending span of 88 ft, similar to that of the CTW100 designs. As with the HWB100, a low-fidelity model is created and high-fidelity trim-constrained drag minimization is performed, with the optimized design referred to as the HWB100D-1. The resulting performance is shown in Table 4 together with that of the CTW100-1 and HWB100-1. All the results presented in this paper correspond to the start of the cruise segment of the nominal mission and include the drag contribution of the vertical stabilizers. Due to the increased span allowed for through span-loading, the HWBs have up to a 15.7% higher lift-to-drag ratio than the CTW100-1; however their higher weight negates much of this benefit such that the HWBs have, at best, about the same drag as the CTW100-1. The Breguet range equation is used to calculate fuel burn for the 500 nmi cruise segment. The CTW100-1 burns 3,244 lb of fuel, while the HWB100D-1 burns 3,264 lb.

The regional-class HWBs presented above have up to 14% *higher* wetted area than the CTW100-1. This motivates the question, which forms the basis for the following section: Is there a different HWB configuration that is more beneficial for smaller aircraft sizes?

[c]The 'D' designator refers to the fact that this configuration now fits in code 'D' gates instead of code 'C'.

**Table 4: Design information for all optimized designs including increased span derivatives. Drag is given relative to the optimized CTW100-1 reference aircraft.**

| Design | Span [ft] | Bending span [ft] | Weight [lb] | $C_L$ [–] | $L/D$ [–] | Relative drag [%] |
|---|---|---|---|---|---|---|
| CTW100-1 | 94 | 85 | 91,500 | 0.481 | 19.8 | — |
| HWB100-1 | 118 | 76 | 103,200 | 0.185 | 22.1 | +1.1 |
| HWB100D-1 | 130 | 88 | 106,600 | 0.186 | 23.0 | +0.3 |

## IV. Exploratory Aerodynamic Shape Optimization

The optimized HWBs in the previous section had higher drag than the CTW100-1, largely due to their higher wetted area and weight. While the optimization possessed significant geometric freedom, the specification of the cabin layout and the resulting cabin shape constraint prevented significant geometric changes being made to the center-body, a large source of wetted area.

To investigate alternative HWB shapes that may offer improved aerodynamic efficiency, an exploratory optimization is performed with the cabin shape constraint removed, resulting in increased geometric freedom. This study aims to find the maximum aerodynamic efficiency of regional-class HWBs. Thus, instead of performing lift-constrained drag-minimization as with the original designs, the optimization objective is to maximize the lift-to-drag ratio. Thus, no lift target is required, and the pitching moment constraint is not considered. This also reduces the computational cost, as only one adjoint solve is now required as compared to the three in the trim-constrained case.

The aim of these studies is to find trends in the optimal shape rather than details. Few constraints are imposed, and these studies are intended to guide a new design which can then take additional requirements into consideration. For example, the resulting shape may have sufficient space in the center-body for the payload, but due to minimum dimension requirements cannot accommodate a practical cabin layout; thus necessitating a manually designed center-body whose shape is guided by the exploratory result.

The starting shape for the optimization is the HWB100. The design variables and constraints for this problem are the same as for the HWB optimizations presented in the previous section, with the notable exceptions that: 1) the HWB center-body is defined up to the wing root, i.e. there is no 'transition' joint, 2) the leading and trailing edges of the body are not required to be straight, and 3) the cabin shape constraint, which is highly restrictive, is replaced with body area and volume constraints. The cabin floor area and usable cabin volume of the baseline HWBs are approximately $770\,\text{ft}^2$ and $5{,}000\,\text{ft}^3$, respectively. The assumption is made that only 50% of the projected area and volume of the body is usable for housing the cabin due to minimum dimension requirements; the area and volume of the body are constrained accordingly. There are a total of 425 effective design variables.

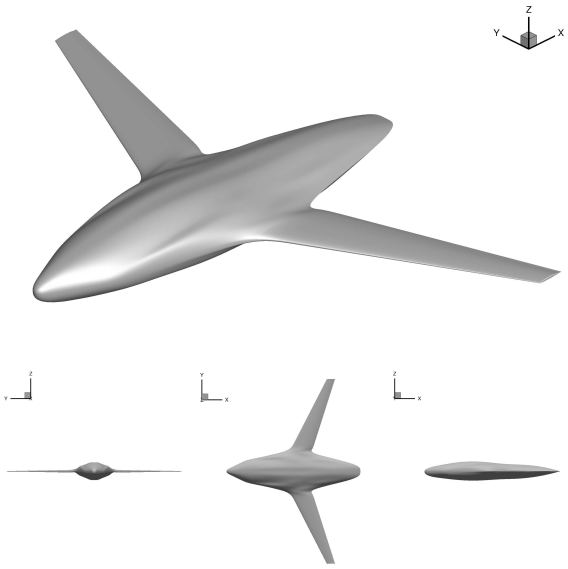

**Figure 10: The resulting shape from the exploratory optimization.**

The optimizer removes all shocks from the design and decreases the wetted area by 9.7%. This results in a lift-to-drag ratio of 26.4; the drag contribution for the vertical fins is not added here. The projected area of the body, as well as the volumes of the body and wing go to their lower bounds. The resulting shape is shown in Figure 10. The optimizer has decreased the body width, with an associated increase in the span of the wing, and increased the slenderness ratio of the body. Several variations of this problem formulation have been investigated, including with various utilization factors for the body area/volume, and by using the same 3-segment span definition which was used for the trim-constrained problems. All of these variations lead to the similar conclusion that for regional-class aircraft the aerodynamically optimal shape consists of a narrow body with a distinct wing.

Since this is a single-discipline optimization, any changes in structural weight caused by changes in span-loading of the payload, and by different cabin shapes are not captured; hence this optimization represents strictly an aerodynamically optimal design. A full aerostructural optimization would be required to capture this weight-drag trade-off in the exploratory optimization.

### A. Lifting-Fuselage Configuration Design

While the exploratory result presented above has sufficient body volume and area to house the required payload, it is not possible to fit a practical cabin shape within the resulting body shape due to minimum dimension requirements. Thus, the result of the exploratory optimization suggests the development of a new configuration, which, by virtue of its lifting center-body and distinct wings, will be referred to generically as a Lifting-Fuselage Configuration (LFC), and specifically, the LFC100. A design based on the geometry shown in Figure 10 is developed, and a cabin layout is designed that fits within the new shape while maintaining

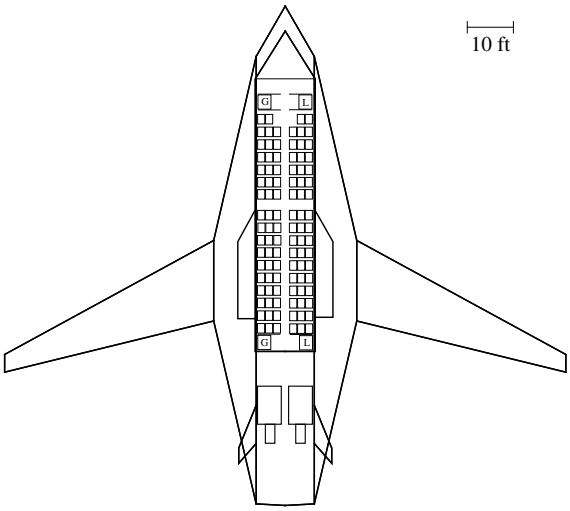


**Figure 11: Baseline LFC100 design.**

**Table 5: Baseline LFC100 design summary.**

| | | |
|---|---|---|
| **Capacity** | | |
| Passengers + crew | 100+5 | |
| Max payload | 28,400 | lb |
| **Geometry** | | |
| Reference area | 3,116 | $ft^2$ |
| Total span | 118 | ft |
| Length | 105 | ft |
| MAC | 67.2 | ft |
| Aspect ratio | 4.5 | |
| **Weight** | | |
| MTOW | 118,700 | lb |
| OEW | 71,100 | lb |
| Wing load at MTOW | 38.1 | $lb/ft^2$ |
| **Nominal mission cruise** | | |
| Range | 500 | nmi |
| Altitude | 36,000 | ft |
| Mach number | 0.78 | |
| Reynolds number | 121 | $\times 10^6$ |
| Weight* | 104,100 | lb |
| $C_L$* | 0.16 | |
| CG location* | 54 | ft |

* At start of cruise

straight walls and a practical seating layout. This results in a 16-row, 3-3 cabin layout, with baggage compartments outboard of the passenger cabin, as shown in Figure 11.

The span of this design is, as with the HWB100, 118 ft. Due to the decreased span-loading caused by the layout of the passenger compartment, the bending span increases relative to the HWB100. The LFC100 has a bending span of 88 ft, the same as the HWB100D and close to that of the CTW100. Thus, while the LFC100 has a larger span than the CTW100, this increase does not come at a prohibitive weight penalty, and it is thus assumed that this span is feasible and produces a fair comparison with the optimized CTW100-1 reference aircraft.

As with the HWB100 designs, a low-fidelity model of the LFC100 is created and shown in Figure 11, with the corresponding design information given in Table 5. Due to the small lateral offset of the engines and the long fuselage, the fins for this design require only about a quarter of the area as for the HWB100. Due to the very small one-engine-inoperative yawing moment for this design, this may no longer be the condition that sizes the fins. Thus, the fin size is increased to provide a margin for directional stability considerations and for acoustic shielding of the engines.

Trim-constrained drag minimization of the LFC100 is performed in the same manner as the original HWBs, and the resulting design is referred to as the LFC100-1. The optimized design is shown in Figure 12, with sectional pressure distributions at a number of span-stations presented in Figure 13. The centerline chord has been reduced by 1% to 104 ft, with a corresponding thickness-to-chord ratio of 9%. The fuselage

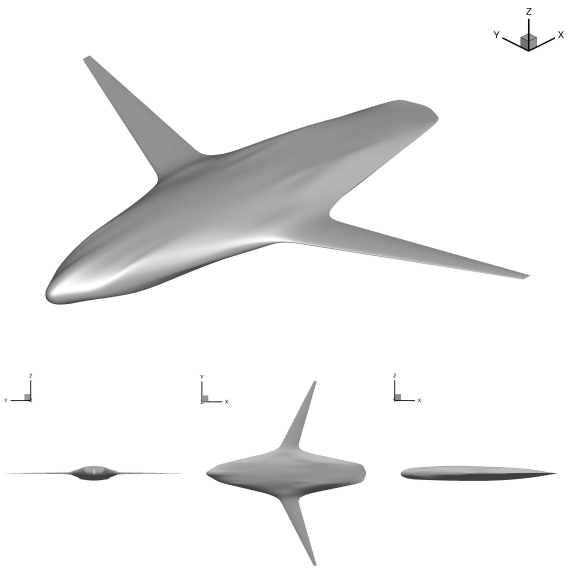

**Figure 12: The optimized LFC100-1 concept.**

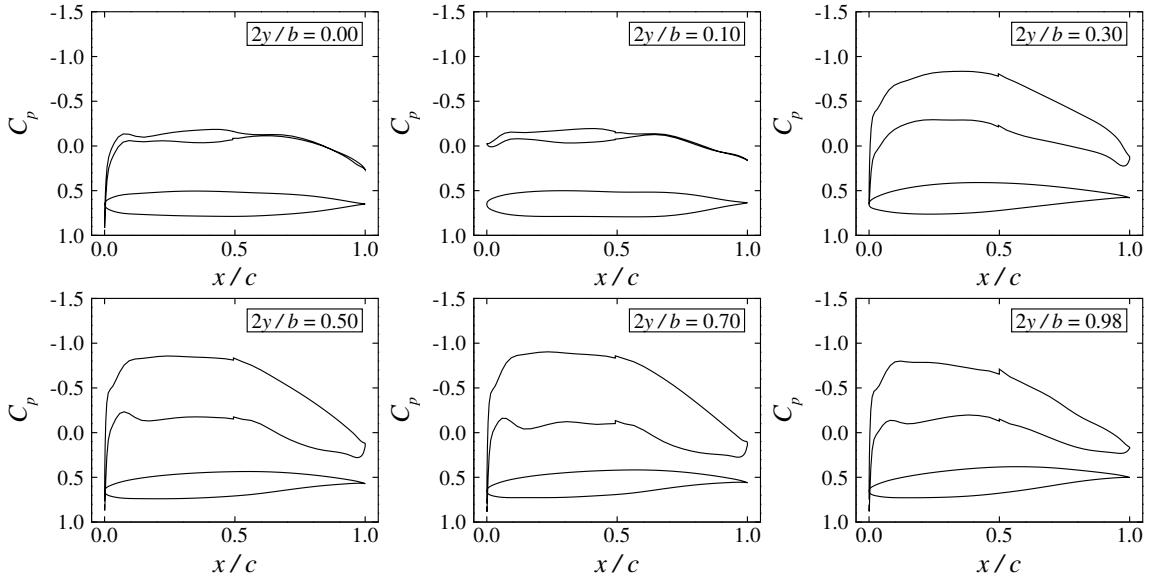


**Figure 13: Pressure distributions at a series of span-stations of the optimized LFC100-1. Station $2y/b = 0.00$ is at the centerline, station $2y/b = 0.10$ is at the outboard edge of the passenger cabin, and the remainder are on the wing.**

carries 31% of the lift. This can be contrasted with the D8 'double-bubble' design in the single-aisle class[52] for which the body carries 20% of the lift. While both configurations rely on increased lift carried by the fuselage, one of the distinguishing features of this design is it maintains a blended transition between the wing and fuselage which relieves the wings, and increases the thickness, and therefore structural depth, near the wing root. The lift-to-drag ratio is 24.0, which results in 6.1% lower drag than the CTW100-1, and 6.4% lower drag than the HWB100D-1. The static margin is $-3.2\%$. The performance of all designs is summarized in Table 6.

**Table 6: Design information for all optimized designs including increased span derivatives. Drag is given relative to the CTW100-1.**

| Design | Span [ft] | Bending span [ft] | Weight [lb] | $C_L$ [–] | $L/D$ [–] | Relative drag [%] |
|---|---|---|---|---|---|---|
| CTW100-1 | 94 | 85 | 91,500 | 0.481 | 19.8 | — |
| HWB100-1 | 118 | 76 | 103,200 | 0.185 | 22.1 | +1.1 |
| HWB100D-1 | 130 | 88 | 106,600 | 0.186 | 23.0 | +0.3 |
| LFC100-1 | 118 | 88 | 104,100 | 0.191 | 24.0 | −6.1 |

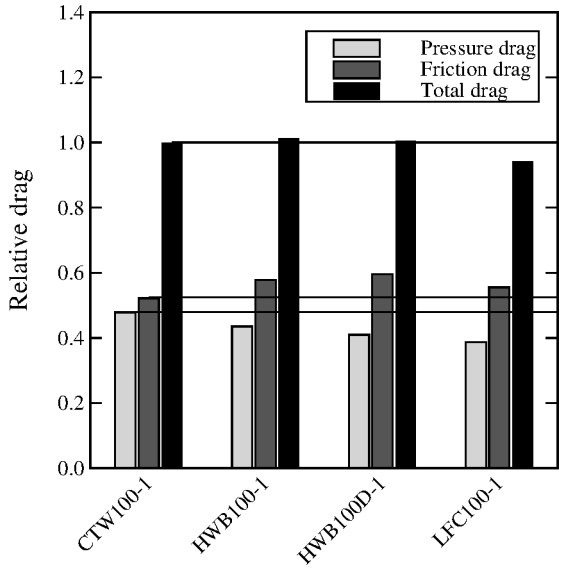


**Figure 14: Breakdown of friction and pressure drag for each design. Drag given relative to that of the CTW100-1 design.**

The breakdown of friction and pressure drag for each design is shown in Figure 14. The original optimized HWBs, HWB100-1 and HWB100D-1, give higher friction drag than the reference aircraft due in large part to their higher wetted area. Pressure drag, primarily composed of induced drag, is lower, but the higher weight and increased friction drag of the HWBs negates much of this potential benefit. The total drag is thus similar to that of the CTW100-1. In contrast, although the LFC100-1 exhibits slightly higher friction drag than the CTW100-1, it shows a large induced drag benefit, leading to a net drag savings of 6.1%. This translates to a similar savings in cruise fuel burn, with total cruise fuel burn of 3,048 lb.

## V. Performance Studies

This section will further investigate the performance potential of the designs studied, including the sensitivity of aerodynamic performance to estimated weight, impact of cruise altitude, and stability requirements. The CTW100, HWB100D, and LFC100 configurations will be studied. The HWB100 design is dropped, as it is postulated that the HWB100D configuration is likely more practical due to its larger span, but is still

**Table 7: Performance of the HWB100D and LFC100 designs with ±10% variability in OEW. Drag is given relative to the CTW100-1 reference aircraft.**

| Design | Relative drag [%] | |
|---|---|---|
| | OEW−10% | OEW+10% |
| HWB100D-1 | −2.5 | +3.6 |
| LFC100-1 | −9.6 | −2.2 |

feasible due to its appropriate bending span.

### A. Sensitivity to Weight

There is large uncertainty in both the center-body weight estimates for both the HWB and LFC designs, as well as the suitability of the low-fidelity weight models used for the airframe weight prediction. As shown in the previous sections, a portion of the improved aerodynamic efficiency of the unconventional configurations is negated by their higher weight, resulting in a drag reduction relative to the CTW100-1 that is significantly less than the lift-to-drag benefit. Thus, a weight sensitivity study is conducted whereby the OEW of the HWB and LFC predicted by the low-fidelity models is perturbed by ±10%. The trim-constrained drag minimization optimizations are then restarted with the new lift targets at the start of cruise. The resulting performance is shown in Table 7.

If the OEW has been over-predicted by the low-fidelity sizing tool by 10%, then all of the unconventional designs offer lower drag than the CTW100-1, up to almost 10% for the LFC100-1. Conversely, if the weight was under-predicted by 10% then only the LFC100-1 offers lower drag than the CTW100-1, although the savings is reduced to 2.2%. Thus, the new LFC concept exhibits high enough aerodynamic efficiency such that, even in the face of still higher weight, it has lower drag than the CTW100-1 reference aircraft.

The HWB pressure vessel model of Bradley[25] is used for the center-body weight estimates for the LFC100 design. However, the cabin shape is significantly different than that for which the model was created. It is also possible that this centerbody layout would be better served by an elliptical or double-bubble type cross section. To address this possibility, the non-cylindrical center-body weight model is replaced with that for a cylindrical pressure vessel. This results in an OEW of 60,300 lbs and an MTOW of 106,300 lbs; compared to 71,100 lbs and 118,700 lbs, respectively, for the original LFC100. This brings the weight of the LFC100 down close to that of the CTW100. Lift-constrained drag minimization is performed with the weight at the start of cruise corresponding to this weight model, resulting in a drag reduction relative to the CTW100-1 of 11.2%.

Both the HWB and LFC concepts, particularly the LFC, offer higher aerodynamic efficiency than the CTW design. Minimizing structural weight as much as possible will thus be critical in obtaining the full

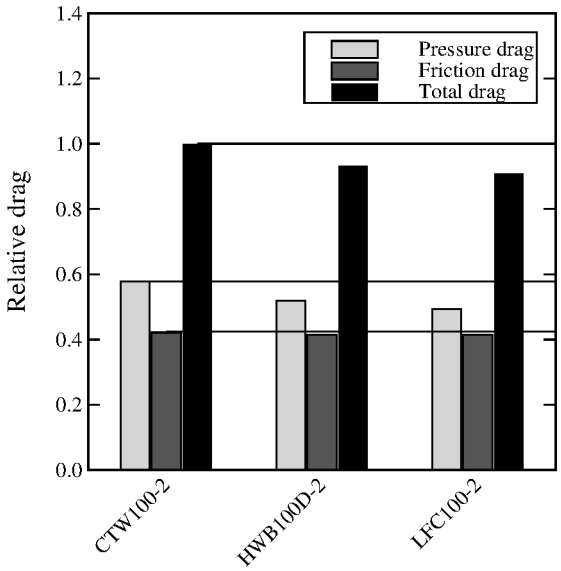


**Figure 15: Breakdown of friction and pressure drag for each design when operating at their optimal altitude. Drag given relative to that of the CTW100-2 design.**

aerodynamic potential of this concept.

### B. Performance at Optimal Altitude

All of the above optimizations were performed at the same altitude of 36,000 ft, i.e. with the unconventional designs operating in existing patterns. However, this is not likely to be the optimal altitude for the HWB or LFC designs due to their lower wing-loading, and as evidenced by the fact that the friction drag shown in Figure 14 is higher than the pressure drag. To address this, optimizations are performed whose objective is to maximize the lift-to-drag ratio using the same design variables and constraints as used previously; however, lift is not constrained. Instead, the lift-to-drag ratio maximization results in the determination of the optimal lift coefficient. The dynamic pressure, and hence altitude, that yields $W = q_\infty C_L S$ is then solved for. This procedure over-predicts the true optimal altitude since the dependence of Reynolds number on altitude is not accounted for. Thus, trim-constrained drag minimization is performed at the altitude predicted by the above procedure and at decrements of 2,000 ft, with the Reynolds number adjusted accordingly and the target lift such that $W = q_\infty C_L S$. The design variables and pitching moment constraint are the same as for the previous optimization cases. This allows for the determination of designs, indicated by the suffix '-2', which operate at their aerodynamically optimal altitude. The CTW100-2 cruises at 42,000 ft, the HWB100D-2 at 46,000 ft, and the LFC100-2 at 44,000 ft. The drag breakdown for these designs is shown in Figure 15, from which it can be seen that the designs are operating closer to the condition for the maximum lift-to-drag ratio, i.e. equal induced and parasitic drag. Note that the pressure drag shown in Figure 15 contains both induced drag, and the form component of parasitic drag.

**Table 8: Design information for all designs at their optimal altitude. Drag is given relative to the CTW100-2, which has 0.5% lower drag than the CTW100-1.**

| Design | Span [ft] | Bending span [ft] | Weight [lb] | Altitude [ft] | $C_L$ [–] | $L/D$ [–] | Relative drag [%] |
|---|---|---|---|---|---|---|---|
| CTW100-2 | 94 | 85 | 91,500 | 42,000 | 0.582 | 19.9 | — |
| HWB100D-2 | 130 | 88 | 106,600 | 46,000 | 0.284 | 24.8 | −6.5 |
| LFC100-2 | 118 | 88 | 104,100 | 44,000 | 0.267 | 24.9 | −9.1 |

The performance of each of these optimized designs is summarized in Table 8, and the HWB100D-2 and LFC100-2 designs are shown in Figure 16 along with the designs optimized for 36,000 ft, HWB100D-1 and LFC100-1. While all of the designs now operate closer to their optimal lift coefficient, the change in lift coefficient, and hence altitude, for the HWB and LFC is greater than for the CTW100-2, such that the change in the lift-to-drag ratio and drag reduction are greater. This is particularly true for the HWB100D-2. At 36,000 ft only the LFC100-1 offers a drag reduction compared to the CTW100-1. Due to the change in altitude, both the HWB100D-2 and LFC100-2 now outperform the CTW100-2, yet the biggest drag reduction, at 9.1%, is still achieved by the LFC100-2. All of the designs considered now operate at significantly higher cruise altitudes. So while these designs are aerodynamically optimal, additional considerations such as the potential increase in engine size, operational implications due to having to climb to such a high altitude for a short-range mission, and the potential weight increase of the pressure vessel, would have to be accounted for in determining the optimal cruise altitude.

### C. Implications of Longitudinal Static Stability

While all of the designs are trimmed, only the CTW100-1 has a positive static margin, although no such constraint was included in the optimization. Both the HWB100D-1 and LFC100-1 have a margin greater than −5% which could be accepted through the use of an active stability system. However, certification challenges would exist with such a design. Thus, the performance impact of requiring a more positive static margin is investigated for the HWB100D-1 and LFC100-1 designs, which have −2.5% and −3.2% margins, respectively. Two trim-constrained drag minimization problems are performed for each design using the same formulation as before but with the addition of 0% and +5% static margin constraints. The static margin constraint is calculated as $K_n = -\frac{\partial C_M}{\partial C_L} \approx -\frac{\Delta C_M}{\Delta C_L}$, via a finite-difference with respect to the angle-of-attack, with a step-size of $\Delta\alpha = 0.1°$. In addition, the CG location is now included as a design variable such that the optimizer can place it to find the optimal trade-off between the trim and static-margin constraints. It is allowed to vary by ±10% of the MAC about the point predicted by the low-fidelity models and used for the previous cases. Changes in the CG location are taken into account in the static margin calculation through the calculation of $C_M$, which uses the current CG location at each iteration. Fixing the CG can potentially

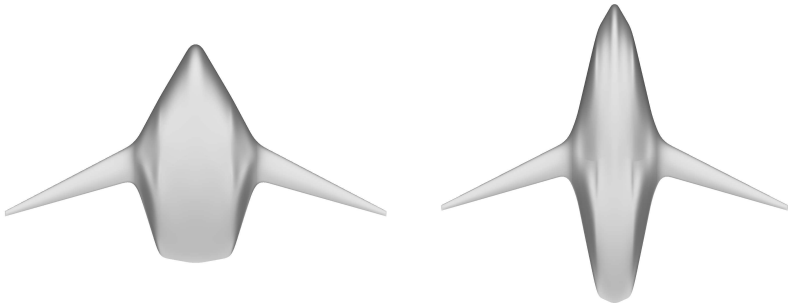

(a) HWB100D-1 (b) LFC100-1

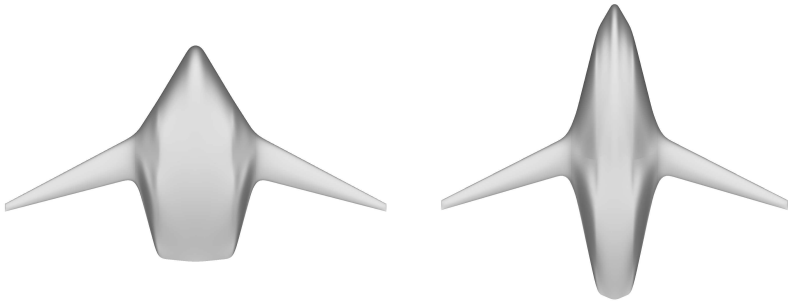

(c) HWB100D-2 (d) LFC100-2

**Figure 16: A comparison of the optimal HWB100D-1 and LFC100-1 designs and the corresponding designs optimized with variable altitude, HWB100D-2 and LFC100-2. All shown to the same scale.**

**Table 9: Design performance when subjected to a static margin constraint. The unconstrained cases are included for reference. Drag is given relative to the CTW100-1.**

| Design | Weight [lb] | $\Delta x_{CG}$* [% MAC] | $K_n$ [% MAC] | $C_L$ [–] | $L/D$ [–] | Relative drag [%] |
|---|---|---|---|---|---|---|
| HWB100D-1 | 106,600 | — | −2.5 | 0.186 | 23.0 | +0.3 |
| HWB100D-3 | 106,600 | −1.3 | 0.0 | 0.186 | 23.0 | +0.3 |
| HWB100D-4 | 106,600 | −6.2 | +5.0 | 0.186 | 22.8 | +1.2 |
| LFC100-1 | 104,100 | — | −3.2 | 0.191 | 24.0 | −6.1 |
| LFC100-3 | 104,100 | −2.5 | 0.0 | 0.191 | 23.8 | −5.4 |
| LFC100-4 | 104,100 | −7.7 | +5.0 | 0.190 | 22.8 | −1.2 |

* Change in CG location. Negative values correspond to forward movement of the CG.

result in an unrealistic performance penalty due to the reduced freedom available to the optimizer, and it is postulated that the CG could be moved within ±10% of the MAC by proper distribution of systems and fuel. The CG is not included as a design variable for the previous cases as it would simply be moved to its aft bound to minimize trim drag. The resulting performance of the optimized designs is shown in Table 9. The suffix '-3' indicates cases with the 0% static margin constraint, and '-4' denotes those cases with the +5% constraint.

In each case the optimizer moves the CG forward with the increasingly positive static margin requirement. This is accompanied by forward movement of the centers of pressure on the center-body to maintain trim, as shown in Figures 17 and 18. For the HWB100D-3, the 0% static margin is obtained by moving the CG

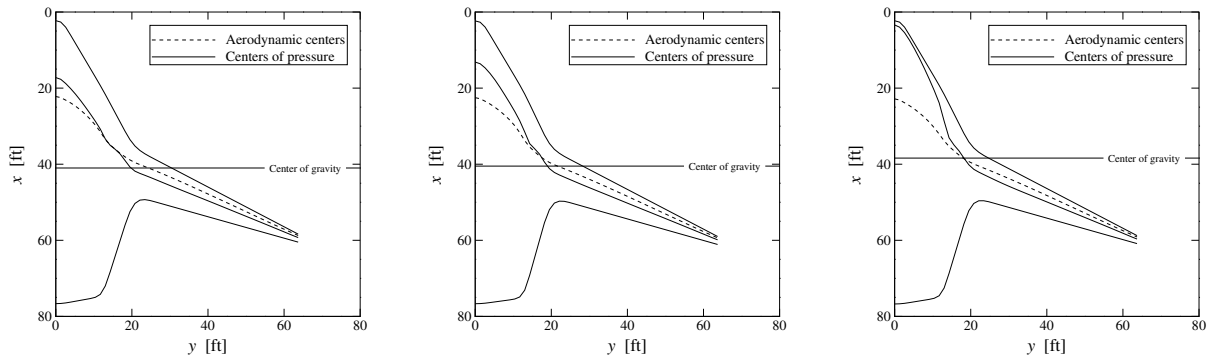


(a) HWB100D-1 (b) HWB100D-3 (c) HWB100D-4

**Figure 17: Spanwise distribution of the centers of pressure and aerodynamic centers for each HWB100D design.**

forward by 1.3% of the MAC, together with a slight aft movement of the wing, and hence aerodynamic centers. For the LFC100-3 the 0% static margin is satisfied primarily by forward movement of the CG and some tailoring of the sections near the wing tip to move the local aerodynamic centers aft. The HWB100D-3 is able to achieve the required static margin with no performance penalty, while the LFC100-3 design sees a slight performance decrement such that its drag reduction relative to the CTW100-1 is reduced from 6.1% to 5.4%. For the +5% static margin cases, the required margin is obtained by moving the CG forward by about 5% of the MAC relative to the 0% margin cases, with an associated forward movement of the centers of pressure on the center-bodies to maintain trim. For the HWB100D-4, the resulting performance penalty is such that this design now has 1.2% higher drag than the CTW100-1. The drag increase for the LFC100-4 causes the drag reduction relative to the CTW100-1 to be reduced to 1.2%. To summarize, for the classically shaped HWBs, there is no drag penalty to increase the static margin to zero and a small penalty to reach +5%. In contrast, the new LFC shape displays a small penalty for the zero margin and a substantial drag penalty for the large positive static margin. Hence the proposed concept is most advantageous if relaxed static stability can be accepted.

## VI. Conclusions

The aerodynamic performance of regional-class HWBs was investigated and compared with equivalent conventional tube-and-wing designs. For regional-class HWBs it was found that 'classically' shaped HWBs do not offer a wetted area reduction, and their primary aerodynamic benefit is the ability to increase the span via span-loading of the payload, although the increased span cannot negate the wetted are increase. A novel regional-class lifting-fuselage configuration was found through high-fidelity RANS-based exploratory aerodynamic shape optimization and features a lifting fuselage with a distinct wing. This concept leads to

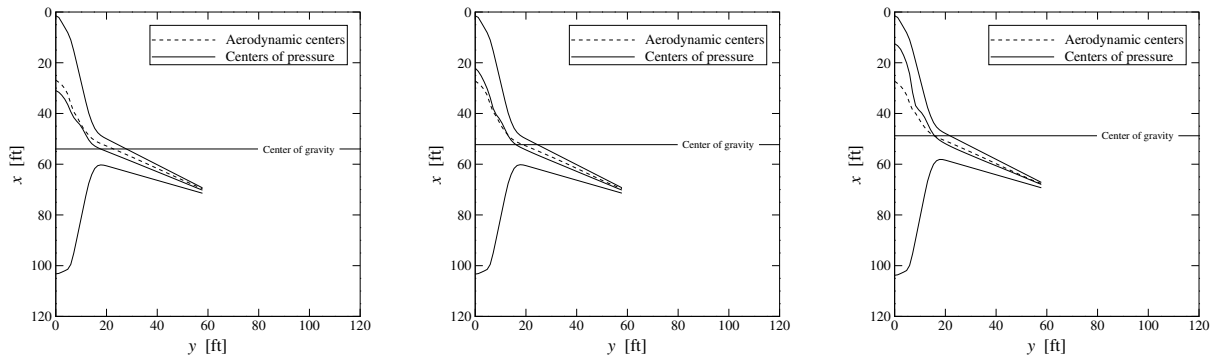


(a) LFC100-1 (b) LFC100-3 (c) LFC100-4

**Figure 18: Spanwise distribution of the centers of pressure and aerodynamic centers for each LFC100 design.**

lower wetted area than a classical HWB for regional-class aircraft. The extent of the span-loading of the payload is reduced compared to the classical shape; however it is still greater than for conventional tube-and-wing designs, thus allowing for a larger span for equivalent bending span. Using this new concept, a regional-class LFC was designed that provides a 6% drag reduction compared to an equivalently optimized conventional design when operating at the same conditions. If the LFC's OEW can be reduced by 10% compared to that estimated here, then the drag savings of the LFC increases to almost 10% compared to the CTW reference aircraft.

When all designs are free to operate at their optimal altitude, the new LFC design maximizes its lift-to-drag ratio at 44,000 ft. At this altitude, the drag reduction of the LFC increases to 9% relative to a CTW at its optimal altitude.

The requirement of increased longitudinal static stability was found to lead to a greater degradation in performance for the new LFC than for the classical HWB shape, particularly for increasing pitch stiffness, yet the novel shape still offered lower drag than the classical HWB.

This study demonstrates that the classical HWB configuration does not offer aerodynamic efficiency gains in the regional-jet segment, but through the use of exploratory aerodynamic shape optimization, a lifting-fuselage configuration was found that offers drag savings of roughly 6-10%. While the lifting-fuselage configuration offers superior aerodynamic performance compared to the conventional aircraft, further studies to investigate stability and control and aeroelastic behaviour, and to improve weight estimation will be required to prove the viability of this concept.

## Acknowledgments

Financial support is provided in part by the Natural Sciences and Engineering Research Council of Canada and the University of Toronto. Computations were performed on the General Purpose Cluster

supercomputer at the SciNet HPC Consortium. SciNet is funded by: the Canada Foundation for Innovation under the auspices of Compute Canada; the Government of Ontario; Ontario Research Fund - Research Excellence; and the University of Toronto.

## References

[1]Liebeck, R. H., "Design of the Blended Wing Body Subsonic Transport," *Journal of Aircraft*, Vol. 41, No. 1, 2004, pp. 10–25.

[2]Hileman, J. I., Spakovszky, Z. S., Drela, M., Sargeant, M. A., and Jones, A., "Airframe Design for Silent Fuel-Efficient Aircraft," *Journal of Aircraft*, Vol. 47, No. 3, 2010, pp. 956–969.

[3]Li, V. and Velicki, A., "Advanced PRSEUS Structural Concept Design and Optimization," *12th AIAA/ISSMO Multidisciplinary Analysis and Optimization Conference*, AIAA-2008-5840, Victoria, BC, September 2008.

[4]Mukhopadhyay, V., Sobieszczanski-Sobieski, J., Kosaka, I., Quinn, G., and Vanderplaats, G. N., "Analysis, Design, and Optimization of Noncylindrical Fuselage for Blended-Wing-Body Vehicle," *Journal of Aircraft*, Vol. 41, No. 4, 2004, pp. 925–930.

[5]Hansen, L. U., Heinze, W., and Horst, P., "Blended Wing Body Structures in Multidisciplinary Pre-Design," *Structural and Multidisciplinary Optimization*, Vol. 38, No. 1, 2008, pp. 93–106.

[6]Vicroy, D. D., "Blended-Wing-Body Low-Speed Flight Dynamics: Summary of Ground Tests and Sample Results," *47th AIAA Aerospace Sciences Meeting and Exhibit*, AIAA-2009-0933, Orlando, FL, January 2009.

[7]Voskuijl, M., La Rocca, G., and Dircken, F., "Controllability of Blended Wing Body Aircraft," *26th International Congress of the Aeronautical Sciences*, Anchorage, AL, September 2008.

[8]Nickol, C. L., "Hybrid Wing Body Configuration Scaling Study," *50th AIAA Aerospace Sciences Meeting and Exhibit*, AIAA-2012-0337, Nashville, TN, January 2012.

[9]Wakayama, S., "Blended-Wing-Body Optimization Problem Setup," *8th AIAA/USAF/NASA/ISSMO Symposium on Multidisciplinary Analysis and Optimization*, AIAA-2000-4740, Long Beach, CA, September 2000.

[10]Hileman, J. I., Spakovszky, Z. S., Drela, M., and Sargeant, M. A., "Airframe Design for "Silent Aircraft"," *45th AIAA Aerospace Sciences Meeting and Exhibit*, AIAA-2007-0453, Reno, NV, January 2007.

[11]Morris, A. J., "MOB: A European Distributed Multi-Disciplinary Design and Optimisation Project," *9th AIAA/ISSMO Symposium on Multidisciplinary Analysis and Optimization*, AIAA-2002-5444, Atlanta, GA, September 2002.

[12]Méheut, M., Grenon, R., Carrier, G., Defos, M., and Duffau, M., "Aerodynamic Design of Transonic Flying Wing Configurations," *CEAS Katnet II Conference on Key Aerodynamic Technologies*, Breme, Germany, May 2009.

[13]Peigin, S. and Epstein, B., "Computational Fluid Dynamics Driven Optimization of Blended Wing Body Aircraft," *AIAA Journal*, Vol. 44, No. 11, 2006, pp. 2736–2745.

[14]Qin, N., Vavalle, A., Le Moigne, A., Laban, M., Hackett, K., and Weinerfelt, P., "Aerodynamic Considerations of Blended Wing Body Aircraft," *Progress in Aerospace Sciences*, Vol. 40, No. 6, 2004, pp. 321–343.

[15]Le Moigne, A. and Qin, N., "Aerofoil Profile and Sweep Optimisation for a Blended Wing-Body Aircraft Using A Discrete Adjoint Method," *The Aeronautical Journal*, Vol. 110, No. 1111, 2006, pp. 589–604.

[16]Mader, C. A. and Martins, J. R. R. A., "Stability-Constrained Aerodynamic Shape Optimization of Flying Wings," *Journal of Aircraft*, Vol. 50, No. 5, 2013, pp. 1431–1449.

[17]Kuntawala, N. B., Hicken, J. E., and Zingg, D. W., "Preliminary Aerodynamic Shape Optimization of a Blended-Wing-Body Aircraft Configuration," *49th AIAA Aerospace Sciences Meeting*, AIAA-2011-0642, Orlando, FL, January 2011.

[18]Lyu, Z. and Martins, J. R. R. A., "Aerodynamic Shape Optimization of a Blended-Wing-Body Aircraft," *51st AIAA Aerospace Sciences Meeting*, AIAA-2013-0283, Grapevine, TX, January 2013.

[19]Lyu, Z. and Martins, J. R. R. A., "Aerodynamic Shape Optimization Studies of a Blended-Wing-Body Aircraft," *Journal of Aircraft*, Vol. 51, No. 5, 2014, pp. 1604–1617.

[20]Reist, T. A. and Zingg, D. W., "Aerodynamic Shape Optimization of a Blended-Wing-Body Regional Transport for a Short Range Mission," *31st AIAA Applied Aerodynamics Conference*, AIAA-2013-2414, San Diego, CA, June 2013.

[21]Osusky, L. and Zingg, D. W., "Application of an Efficient Newton-Krylov Algorithm for Aerodynamic Shape Optimization Based on the Reynolds-Averaged Navier-Stokes Equations," *21st AIAA Computational Fluid Dynamics Conference*, AIAA-2013-2584, San Diego, CA, June 2013.

[22]Torenbeek, E., *Synthesis of Subsonic Airplane Design*, Delft University, 1976.

[23]"Aircraft Design: Synthesis and Analysis," http://adg.stanford.edu/aa241/AircraftDesign.html, December 2014.

[24]Raymer, D. P., *Aircraft Design: A Conceptual Approach*, American Institute of Aeronautics and Astronautics, 5th ed., 2012.

[25]Bradley, K. R., "A Sizing Methodology for the Conceptual Design of Blended-Wing-Body Transports," Tech. Rep. NASA/CR-2004-213016, NASA/Langley Research Center: Joint Institute for Advancement of Flight Sciences, 2004.

[26]Embraer Commercial Aircraft, *Embraer 190 Airport Planning Manual*, 2005, (Revision 10 - 18 February 2013).

[27]General Electric Aviation, *CF34-10E Turbofan Propulsion System*.

[28]Gagnon, H. and Zingg, D. W., "Geometry Generation of Complex Unconventional Aircraft with Application to High-Fidelity Aerodynamic Shape Optimization," *21st AIAA Computational Fluid Dynamics Conference*, AIAA-2013-2850, San Diego, CA, June 2013.

[29]Hicken, J. E. and Zingg, D. W., "A Parallel Newton-Krylov Solver for the Euler Equations Discretized Using Simultaneous Approximation Terms," *AIAA Journal*, Vol. 46, No. 11, 2008, pp. 2773–2786.

[30]Osusky, M. and Zingg, D. W., "A Parallel Newton-Krylov-Schur Flow Solver for the Navier-Stokes Equations Discretized Using Summation-By-Parts Operators," *AIAA Journal*, Vol. 51, No. 12, 2013, pp. 2833–2851.

[31]Hicken, J. E. and Zingg, D. W., "Aerodynamic Optimization Algorithm with Integrated Geometry Parameterization and Mesh Movement," *AIAA Journal*, Vol. 48, No. 2, 2010, pp. 401–413.

[32]Gill, P. E., Murray, W., and Saunders, M. A., "SNOPT: An SQP Algorithm for Large-Scale Constrained Optimization," *Society for Industrial Applied Mathematics Review*, Vol. 47, No. 1, 2005, pp. 99–131.

[33]Osusky, L., Buckley, H., Reist, T., and Zingg, D. W., "Drag Minimization Based on the Navier-Stokes Equations Using a Newton-Krylov Approach," *AIAA Journal*, Vol. 53, No. 6, 2015, pp. 1555–1577.

[34]Osusky, M., Boom, P. D., and Zingg, D. W., "Results from the Fifth AIAA Drag Prediction Workshop obtained with a parallel Newton-Krylov-Schur flow solver discretized using summation-by-parts operators," *31st AIAA Applied Aerodynamics Conference*, AIAA-2013-2511, San Diego, CA, June 2013.

[35]Gagnon, H. and Zingg, D. W., "Two-Level Free-Form and Axial Deformation for Exploratory Aerodynamic Shape Optimization," *AIAA Journal*, Vol. 53, No. 7, 2015, pp. 2015–2026.

[36]Zingg, D. W., Nemec, M., and Pulliam, T. H., "A Comparative Evaluation of Genetic and Gradient-Based Algorithms Applied to Aerodynamic Optimization," *European Journal of Computational Mechanics*, Vol. 17, No. 1, 2008, pp. 103–126.

[37]Chernukhin, O. and Zingg, D. W., "Multimodality and Global Optimization in Aerodynamic Design," *AIAA Journal*, Vol. 51, No. 6, 2013, pp. 1342–1354.

[38]Hicken, J. E. and Zingg, D. W., "A Simplified and Flexible Variant of GCROT for Solving Nonsymmetric Linear Systems," *SIAM Journal of Scientific Computing*, Vol. 32, No. 3, 2010, pp. 1672–1694.

[39]Telidetzki, K., Osusky, L., and Zingg, D. W., "Application of Jetstream to a Suite of Aerodynamic Shape Optimization Problems," *52nd Aerospace Sciences Meeting*, AIAA-2014-0571, National Harbor, MD, January 2014.

[40]Lee, C., Koo, D., Telidetzki, K., Buckley, H., Gagnon, H., and Zingg, D. W., "Aerodynamic Shape Optimization of Benchmark Problems Using Jetstream," *53rd AIAA Aerospace Sciences Meeting*, AIAA-2015-0262, Kissimmee, FL, January 2015.

[41]Koo, D. and Zingg, D. W., "Progress in Aerodynamic Shape Optimization Based on the Reynolds-Averaged Navier-Stokes Equations," *54th Aerospace Sciences Meeting*, AIAA-2016-1292, San Diego, CA, January 2016.

[42]Hicken, J. E. and Zingg, D. W., "Induced Drag Minimization of Nonplanar Geometries Based on the Euler Equations," *AIAA Journal*, Vol. 48, No. 11, 2010, pp. 2564–2575.

[43]Leung, T. M. and Zingg, D. W., "Aerodynamic Shape Optimization of Wings Using a Parallel Newton-Krylov Approach," *AIAA Journal*, Vol. 50, No. 3, 2012, pp. 540–550.

[44]Leung, T. M. and Zingg, D. W., "Design of Low-Sweep Wings for Maximum Range," *29th AIAA Applied Aerodynamics Conference*, AIAA-2011-3178, Honolulu, HI, June 2011.

[45]Gagnon, H. and Zingg, D. W., "High-Fidelity Aerodynamic Shape Optimization of Unconventional Aircraft through Axial Deformation," *52nd Aerospace Sciences Meeting*, AIAA-2014-0908, National Harbor, MD, January 2014.

[46]Reist, T. A. and Zingg, D. W., "Optimization of the Aerodynamic Performance of Regional and Wide-Body-Class Blended Wing-Body Aircraft," *33rd AIAA Applied Aerodynamics Conference*, AIAA-2015-3239, Dallas, TX, June 2015.

[47]Zhang, Z. J., Khosravi, S., and Zingg, D. W., "High-Fidelity Aerostructural Optimization with Integrated Geometry Parameterization and Mesh Movement," *56th AIAA/ASCE/AHS/ASC Structures, Structural Dynamics, and Materials Conference*, AIAA-2015-1132, Kissimmee, FL, January 2015.

[48]Khosravi, S. and Zingg, D. W., "A Numerical Optimization Study on Winglets," *15th AIAA/ISSMO Multidisciplinary Analysis and Optimization Conference*, AIAA-2014-2173, Atlanta, GA, June 2014.

[49]Mavriplis, D. J., Vassberg, J. C., Tinoco, E. N., Mani, M., Brodersen, O. P., Eisfeld, B., Wahls, R. A., Morrison, J. H., Zickuhr, T., Levy, D., and Murayama, M., "Grid Quality and Resolution Issues from the Drag Prediction Workshop Series," *Journal of Aircraft*, Vol. 46, No. 3, 2009, pp. 935–950.

[50]Buckley, H. P. and Zingg, D. W., "An Approach to Aerodynamic Design Through Numerical Optimization," *AIAA Journal*, Vol. 51, No. 8, 2013, pp. 1972–1981.

[51]Sargeant, M. A., Hynes, T. P., Graham, W. R., Hileman, J. I., Drela, M., and Spakovszky, Z. S., "Stability of Hybrid-Wing-Body Aircraft with Centerbody Leading-Edge Carving," *Journal of Aircraft*, Vol. 47, No. 3, 2010, pp. 970–974.

[52]Drela, M., "Development of the D8 Transport Configuration," *29th AIAA Applied Aerodynamics Conference*, AIAA-2011-3970, Honolulu, HI, June 2011.